Measuring Mechanical Behavior of Steel During Solidification: Modeling the SSCC Test

MATTHEW ROWAN, BRIAN G. THOMAS, ROBERT PIERER, and CHRISTIAN BERNHARD

The submerged split chill contraction (SSCC) test can measure forces in a solidifying steel shell under controlled conditions that match those of commercial casting processes. A computational model of this test is developed and applied to increase understanding of the thermal-mechanical behavior during the initial solidification of steel. Determining the stress profile is difficult because of the complicated geometry of the experimental apparatus and the nonuniform temperature and strength across the shell. The two-dimensional axisymmetric elastic-viscoplastic finite-element model of the SSCC test features different mechanical properties and constitutive equations for delta-ferrite and austenite that are functions of both the temperature and the strain rate. The model successfully matches measurements of (1) temperature history, (2) shell thickness, (3) solidification force, and (4) failure location. In addition, the model reveals the stress and strain profiles through the shell and explains what the experiment is actually measuring. In addition to the strength of the shell, the measured force is governed by the strength of the junction between the upper and lower test pieces and depends on friction at the shell–cylinder interface. The SSCC test and the validated model together are a powerful analysis tool for mechanical behavior, hot tear crack formation, and other phenomena in solidification processes such as continuous casting.

DOI: 10.1007/s11663-010-9470-5

I. INTRODUCTION

FUNDAMENTALLY based computational models are useful tools for understanding and solving problems in commercial casting processes. Finding the material properties needed for the models requires controlled laboratory experiments. This work combines these two tools to gain new insight into both the mechanical behavior of a solidifying steel shell and the experiments used to measure that behavior.

The submerged split chill contraction (SSCC) test is a controlled laboratory experiment to measure the force generated in a steel shell as it solidifies and contracts around a solid cylinder that is suddenly immersed in molten steel.[1] This test, pictured in Figure 1, is a simplified form of the submerged split chill tensile (SSCT) experiment developed by Ackerman *et al.*, and since applied by Hiebler and coworkers.[2–4]

The SSCC test body consists of two separate solid-steel pieces shown in Figure 2. Most of the outer surface of both bodies is sprayed with a 0.4 ± 0.02-mm ZrO_2 layer to control the heat flux to match the heat-transfer conditions found in continuous casting. A steel shell solidifies with the primary dendrite growth direction perpendicular to the interface. The relative vertical position of the tops of the two pieces is held constant by a servohydraulic cylinder.

During solidification, a load cell measures the vertical force that is needed to maintain the vertical positions of the pieces. This force generates membrane stresses in the shell across the dendrites with the same orientation experienced in commercial casting processes. After ~25 seconds, the test body is removed from the melt. This removal causes the axial force to decrease to zero, so subsequent contraction causes shrinkage stresses to increase mainly in the radial and circumferential directions. After cooling to room temperature, the shell is detached, cut, and analyzed metallographically for hot-tear cracks. This test is highly repeatable[5] and has been used to investigate force–time[6] and stress–strain[2–7] relationships, shell strength[8] microstructure morphology,[7,9,10] and various defects for many different steel compositions,[1] other castable metal alloys,[11] and cooling rates.[12]

Unfortunately, the SSCC experiment yields little information about its fundamental operation, including what force is being measured, and its relationship to the high-temperature thermal-mechanical behavior of the solidifying steel that is sought. The measured force is a single time-varying scalar taken at a single location far away from the steel shell that forms at the interface of a complex 3D structure. How the local temperature,

MATTHEW ROWAN, formerly Ph.D. Student, Department of Mechanical Science and Engineering, University of Illinois at Urbana-Champaign, Urbana, IL 61801, is now Sr. Associate Engineer with Caterpillar Inc., Technical Center, Mossville, IL 61552-7547. Contact e-mail: Rowan_Matthew_I@cat.com BRIAN G. THOMAS, Professor, is with the Department of Mechanical Science and Engineering, University of Illinois at Urbana-Champaign. ROBERT PIERER, Research Associate, and CHRISTIAN BERNHARD, Associate Professor, are with the Department of Metallurgy, Christian Doppler Laboratory for Metallurgical Fundamentals of Continuous Casting Processes (MCC), University of Leoben, A-8700 Leoben, Austria.

Manuscript submitted October 9, 2010.
Article published online May 7, 2011.

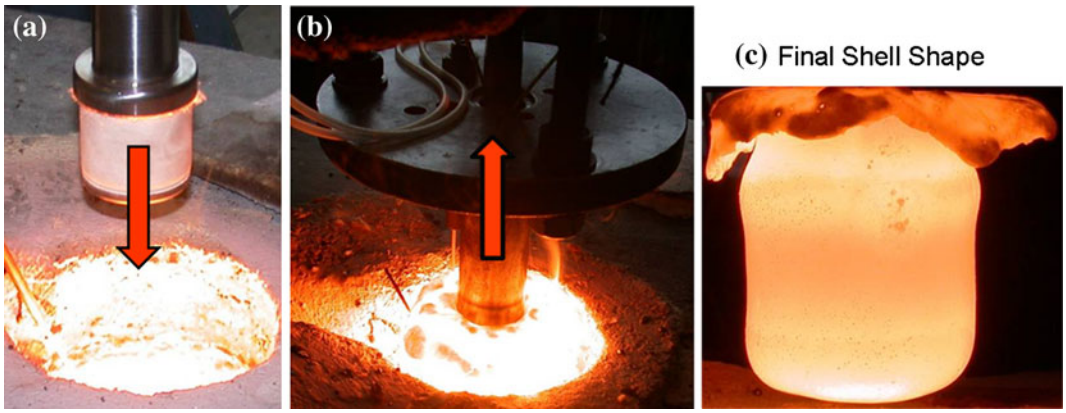

Fig. 1—SSCC test: (*a*) immersion of test body assembly, (*b*) extraction, and (*c*) final shape of solidified shell.

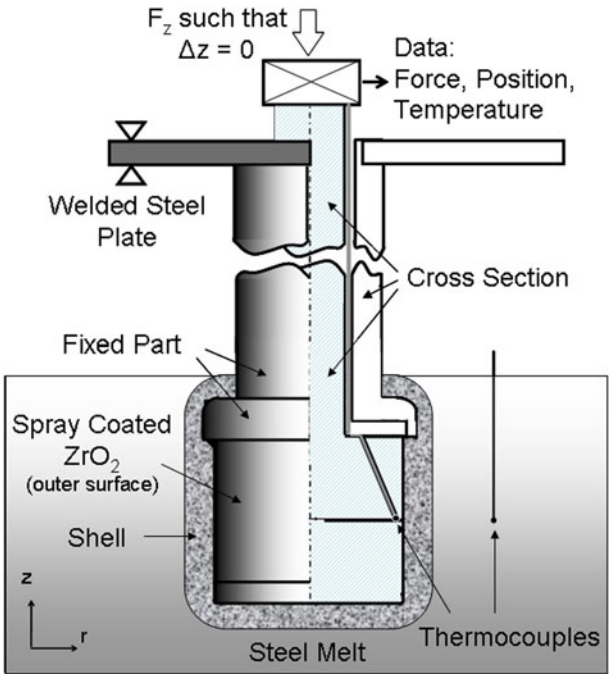

Fig. 2—Schematic representation of the SSCC test.

strain, and stress profiles evolve within the shell and lead to hot-tear cracks cannot be determined using only this test.

In this article, a transient finite-element model of the SSCC test is developed and applied to gain a better understanding of the thermal-mechanical behavior of steel during initial solidification. Separate constitutive models of the thermal-mechanical behavior for austenite[13] and delta-ferrite[12] were developed previously by empirically fitting measured data[14,15] to determine the relationship among stress, strain, strain rate, temperature, and carbon content. These models for the separate phases were incorporated into an efficient numerical methodology of modeling solidification developed by Koric and Thomas[16] and implemented into the commercial software ABAQUS (Providence, RI).[17] This modeling approach has been used for a wide range of applications including stress development in solidifying steel[16] and the formation of longitudinal face cracks.[18] However, the constitutive equations were developed based on tensile test and creep experiments on solid steel that was reheated after solidification and cooling. The differences relative to the mechanical properties during solidification are unknown.

By calibrating the computational model to match the temperature and force measurements of the SSCC test, additional insights can be gained into initial solidification that are more powerful than either of these two tools used separately.

II. PREVIOUS EXPERIMENTS

Attempts to understand the behavior of solidifying steel have been ongoing for centuries. Methodologies been developed only recently to quantify its thermal-mechanical properties and to predict the formation of defects, using both measurements and computational models.

Initial efforts applied standard mechanical tests to reheated solid samples, including high-temperature tensile tests[14,15] and creep tests.[19,20] Wray conducted tensile tests on steel heated in a vacuum furnace from room temperature for both austenite from 1223 K to 1623 K (950 °C to 1350 °C)[14] and delta-ferrite from 1473 K to 1798 K (1200 °C to 1525 °C)[15] at strain rates ranging from 10^{-5} to 10^{-2} s^{-1}. Strength decreased exponentially with increasing temperature toward the solidus and at lower strain rates[14,15] in accordance with observations of other metals.[21–26] Austenite was shown to have much higher strength than delta-ferrite at the same temperature and strain rate.[14,15]

Creep tests on reheated steel samples have been performed primarily to investigate bulging during continuous casting.[19,27] In creep tests by Suzuki *et al.*, 5-mm diameter cylindrical test specimens were machined from as cast-steel and subjected to constant stress levels of 4.1 to 9.8 MPa and temperatures of 1523 K to 1673 K (1250 °C to 1400 °C) for ~1000 seconds.[20,28]

The direction of loading with respect to dendrite growth direction did not have an effect on the creep curves.[28] Austenite recrystallization was observed at 1623 K (1350 °C) at 7.1 MPa at which strains greater than 0.1 were produced.[28]

Because the microstructure experienced during solidification differs from reheated samples, better *in situ* testing methods were developed to measure mechanical behavior of metal during solidification. The punch press or "melt-bending" test[29–31] uses a mold with a removable water-cooled copper plate as one side. The liquid metal cools to begin forming a shell, the copper plate is then removed, and the shell is deformed by a cylinder at strain rates of 10^{-3} to 10^{-2} s^{-1} for specific durations. The cylinder pressure is measured by a DMS pressure transducer and the cylinder movement by an inductive displacement transducer. However, analysis has been simplistic, as strain at the solidification front and force are estimated as follows from the imposed deflection using simple beam bending theory:

$$F = \frac{192EI\delta_{\max}}{l^3} \quad [1]$$

where F is force, E is the elastic modulus, I is the moment of inertia, $\delta_{\max}$ is the maximum displacement, and l is the restrained length. Although such *in situ* tests are useful for quantifying hot-tear cracking, the forces needed to quantify the stress profiles in the solidifying shell have not been recorded. Moreover, the great range of temperatures across the ingot would cause the measured forces to be dominated by low-temperature mechanical properties.

Mizukami *et al.*[32] used a high-temperature tensile apparatus setup in a vacuum, connected to a load cell and high-speed video camera to measure the strength and deformation of steel with varying carbon contents. The samples were reheated, melted, and tested during solidification. The tensile strength was concluded to depend on the phase (austenite or ferrite) present, and the strain is concentrated in the phase with the lowest tensile strength and elongation. These observations agree with other researchers.[21–26]

An experiment designed to quantify the mechanical behavior of a solidifying shell was developed by Ackermann *et al.*[11] This group pioneered the two-piece SSCT test by plunging water-cooled copper cylinders directly into an aluminum melt. After allowing time for the growing shell to reach a desired thickness, the two pieces of the cylinder were separated, which applied a tensile load perpendicular to the direction of primary dendrite arm growth. This allowed measurement of the strength near the two-phase liquid–solid region. Ackermann found considerable strength for solid fractions greater than 0.95 and virtually no strength below this solid fraction.

The most sophisticated experimental apparatus to determine the strength of a solidifying shell was accomplished by Hiebler and coauthors.[33–35] Their SSCT test is a refined version of Ackermann's experiment with better repeatability. It also has been used to determine the susceptibility of forming hot-tear cracks for steels with a wide range of carbon and other alloying content.[1,36,37] Bernhard and coworkers compared SSCT test results with other measurements of thermomechanical behavior of reheated solid samples. The tensile strength near the solidus temperature was approximately 50 pct less than other measurements for austenite[38,39] because the SSCT test is more sensitive to effects of segregation. Tests involving delta-ferrite matched measurements made by Wray,[15] which was attributed to the negligible sensitivity of delta-ferrite to microstructural effects.

All of these tests reveal only a single measurement in regard to the complex multidimensional, multiscale mechanical behavior during solidification of a steel shell. Only by developing a realistic mathematical model of this behavior, including its spatial and time variations, can the experimental measurement be translated into real understanding.

A. *Hot Tearing*

Cracks can occur in steel because of tensile stress combined with any of several different embrittelement mechanisms, which span a wide range of temperatures. Hot tearing is distinct in that it develops near the solidus temperature[40] as a result of strain concentration in the liquid phase between dendrites that cannot be accommodated by liquid feeding. Hot tearing affects all alloys but increases with increasing difference between the liquidus and solidus temperatures.[41] It is aggravated by the partitioning of alloying elements *via* segregation during solidification. Segregation, in turn, is worsened by the slow diffusion in the solid phase, relative to the liquid, and results in small-scale compositional variations. The result is local suppression of the solidus temperature, which increases the size of the two-phase liquid–solid region and makes the steel more susceptible to forming hot tears.

Owing to the great complexity of the phenomena that result in hot tearing, a fundamental theory to predict this defect is too difficult. Thus, research has focused instead on developing simple empirical models to predict hot-tear formation based on fitting experimental measurements.

Rappaz[42] proposed a hot-tearing criterion with the physical basis of when the applied tensile stress causes pressure in the liquid in the two-phase liquid–solid region drops low enough to nucleate voids because of cavitation. Other simpler, less physically realistic criteria, such as those postulated by Clyne and Davies,[43] Feurer,[44] and Katgerman,[45] include the effects of phase fractions, casting conditions, and calculation of the temperature zone most likely to form hot tears. Other criteria are derived from empirically fitting experimental data to determine strain,[46–49] strain rate,[42,50–55] and stress[8,46,56–58] levels that coincide with hot-tear formation.

Pierer *et al.*[8] compared stress-based[59] strain-based[60] strain–rate-based,[61] and the Clyne and Davies model[62] with experimental data from SSCT

tests. He found that, even though each criterion approaches the problem from a different perspective, the predictions of cracking susceptibility are nearly the same.

III. PREVIOUS THERMAL-MECHANICAL MODELS

Initial endeavors to apply computational modeling to the high-temperature thermal-mechanical behavior of steel solidification began with a semianalytical solution of the elastic–plastic behavior of a semi-infinite steel plate prevented from bending[63] as well as with models of the thermal stresses that develop in the shell in and below the mold.[64,65] Computational modeling evolved to more complex behavior including coupling the heat conduction and mechanical equilibrium equations with creep[66,67] and elasticviscoplastic behavior.[16,68–72] Koric and Thomas and coauthors implemented the Kozlowski III model for austenite[13] and the Zhu model for delta-ferrite[68] into both implicit[16] and explicit[73] integration schemes to model the high-temperature behavior of steel. These models have been applied to predict crack formation during continuous casting.[18]

Several computational models of the SSCT[7] and SSCC[1] tests have been performed to study phenomena such as shell strength,[74,75] grain size,[9] hot tearing,[1,10,37,76] and to evaluate proposed constitutive models.[12] Because of the complexity of the phenomena, many aspects of the test are still not fully understood.

IV. EXPERIMENTAL METHODOLOGY

In this work, SSCC experiments on steel solidification were performed at the Christian Doppler Laboratory, University of Leoben (Leoben, Austria).[1] A photograph and schematic of the SSCC test body is given in Figure 1. The test body consists of two main pieces. The "lower part" comprises two stacked cylinders on a common centerline. The larger lower cylinder has a radius of 26 mm and length of 48 mm and is spray-coated with a 0.4-mm-thick ZrO_2 layer to control the heat flux to levels experienced in commercial continuous casting processes. The smaller upper cylinder of the lower part has a radius of 10 mm and a length of 98 mm. The second major piece is a geometrically complex "upper part." The dimensions of both parts are given in appendix

The top surface of the upper part is welded to a fixed steel plate with a hole through which the smaller upper cylindrical portion of the lower part can move. A servohydraulic loader controls the alignment of these two parts. A gap of 4 mm separates the large radius of the lower part from the inner wall of the upper part sleeve.

The assembly of the upper and lower parts, initially at room temperature, is immersed in molten steel, causing a shell to solidify normal to the external surface and at the melt–air interface as shown in Figures 2(a) through (c). During the experiment, the temperature at the SSCC cylinder–steel melt interface decreases causing a shell to form and subsequently desire to shrink as a result of thermal contraction. However, being in contact with the heating and expanding test body, shrinkage of the solidifying shell is prevented. The net force exerted by the solidifying shell lifts up on the lower part and pulls down on the upper part, but the servohydraulic loader prevents any vertical motion. The force required to maintain the relative positions of the upper and lower parts is applied by the servohydraulic loader and is the measured "solidification force."

Four thermocouples record temperature histories at different locations; two are located inside the test body 2 mm from the steel melt interface, whereas the other two are located in the steel melt approximately 20- to 25-mm away from this interface. Each pair of thermocouples is positioned on opposite sides of the test cylinder 180 deg apart. The pour temperature was measured prior to immersing the SSCC test body into the steel melt and was superheated 293 K (20 °C) above the liquidus temperature.

The test body is immersed for a period of approximately 20 to 30 seconds. Then the test body along with the attached steel shell is removed from the melt and cooled to room temperature. This process is shown in Figures 2(a) through (c). The shell is then detached from the test body and cut into 16 separate pieces, 8 from each half, as shown in Figure 3. The shell thickness is measured at multiple locations per sample and then microanalyzed to determine whether any defects are present. The steel melt alloy analyzed in this study is given in Table I.

V. COMPUTATIONAL MODEL

A transient two-dimensional finite-element model of the entire SSCC test has been developed at the Metals Processing Simulation Laboratory at the University of Illinois (Urbana-Champaign, IL), taking advantage of the cylindrical symmetry of the process. It consists of separate heat-transfer and mechanical models of both test body pieces, the solidifying steel shell, and the surrounding liquid.

A. *Heat Conduction Model Governing Equations*

Heat transfer in the test body and the shell is governed by the energy conservation equation. The transient heat conduction model is two-dimensional axisymmetric, with a Lagrangian reference frame (no material velocities) and no heat generation and is governed by the following equation:

$$\rho c_p' \left(\frac{\partial T}{\partial t} \right) = \left(\frac{1}{r} \frac{\partial}{\partial r} \left(rk \frac{\partial T}{\partial r} \right) + \frac{\partial}{\partial z} \left(k \frac{\partial T}{\partial z} \right) \right) \qquad [2]$$

where ρ is the temperature-dependent density, c_p' is the temperature and solid fraction-dependent specific heat, T is temperature, t is time, k is the temperature-dependent thermal conductivity, r is the radial coordinate,

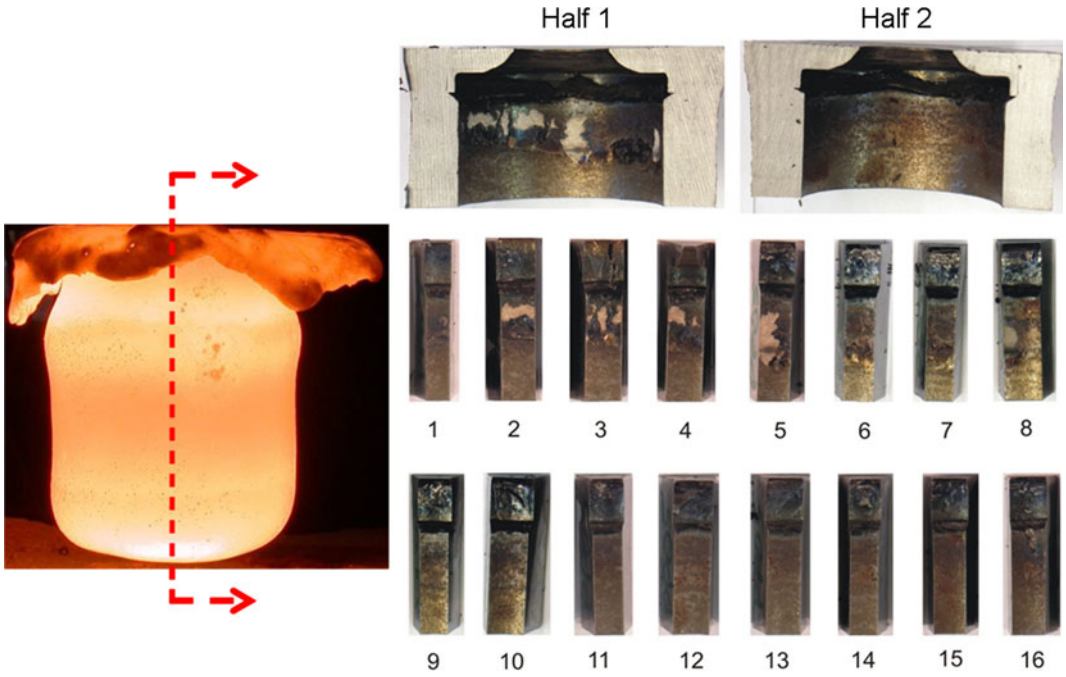

Fig. 3—Illustration of shell cutting for analysis.

Table I. Composition of Experimental Steel Alloy (Weight Percent)

Pct C	Pct Mn	Pct S	Pct P	Pct Si	Pct Al	Pct Fe
0.315	1.44	0.0051	0.0039	0.356	0.0715	Balance

and z is the vertical coordinate. The latent heat effects during solidification are included as an adjustment to the specific heat term as a function of solid fraction when cooling between the liquidus and solidus temperatures according to the following equation:

$$c_p' = c_p - L_f \frac{df_s}{dT} \quad [3]$$

where c_p is obtained from Eq. [A3] in the appendix, L_f is the latent heat, assumed to be 271,000 J/kg, and f_s is the solid fraction.

B. *Mechanical Model Governing Equations*

Strains that develop during solidification are small, so the small strain assumption is used for formulating the mechanical behavior. The linearized strain tensor is expressed as follows:

$$\varepsilon = \frac{1}{2}\left[\nabla \vec{u} + (\nabla \vec{u})^T\right] \quad [4]$$

The spatial displacement gradient $\nabla \vec{u} = \partial u/\partial r$ is small, and the Cauchy stress tensor is balanced by the body forces b according to the initial configuration of the material as follows:

$$\nabla \times [\sigma] + b = 0 \quad [5]$$

Details of the derivation of these material states are given elsewhere.[18]

The total strain rate is represented by summation inclusion of the elastic, inelastic (plastic + creep), and thermal components as follows:

$$\dot{\varepsilon} = \dot{\varepsilon}_{\text{elastic}} + \dot{\varepsilon}_{\text{inelastic}} + \dot{\varepsilon}_{\text{thermal}} \quad [6]$$

The stress rate depends on the elastic strain rate only for this particular case in which large rotations are negligible and the material having a linear isotropic behavior and is expressed as follows:

$$\dot{\sigma} = \underline{\underline{D}} : (\dot{\varepsilon} - \dot{\varepsilon}_{\text{inelastic}} - \dot{\varepsilon}_{\text{thermal}}) \quad [7]$$

where $\underline{\underline{D}}$ is the fourth order isotropic tensor of elasticity and is defined as follows:

$$\underline{\underline{D}} = 2\mu \underline{\underline{I}} + \left(k_B - \frac{2}{3}\mu\right) I \otimes I \quad [8]$$

with μ and k_B being the temperature-dependent shear and bulk modulus, respectively, $\underline{\underline{I}}$ and I are the fourth- and second-order identity tensors.

C. *Determination of the Thermal Strain*

Volume changes caused by temperature differences and phase transformations must be considered. The thermal strain tensor is expressed as follows:

$$(\varepsilon_{\text{thermal}})_{ij} = \int_{T_0}^{T} \alpha(T) dT \delta_{ij} \quad [9]$$

where $\alpha(T)$ is the temperature-dependent coefficient of thermal expansion, T_0 is the reference temperature, and δ_{ij} is the Kronecker delta.

The thermal expansion coefficient is found by computing the slope of the thermal linear expansion (TLE) *vs* temperature curve. The reference temperature was chosen to be 573 K (300 °C) with a reference TLE of -1.66×10^{-2}(–). The thermal expansion coefficient is defined as follows:

$$\alpha = \frac{\mathrm{TLE}_{\mathrm{ref}} - \mathrm{TLE}(T)}{T_{\mathrm{ref}} - T} \qquad [10]$$

D. *Determination of the Inelastic Strain*

The elasticviscoplastic response of the solidifying steel shell is modeled by using separate constitutive equations to calculate the inelastic strain rate in the liquid, delta-ferrite, and austenite phases.

The delta ferrite model[68] is a power law empirical fit that relates the stress σ, inelastic strain $\varepsilon_{\mathrm{inelastic}}$, temperature T, carbon content, pct C, and several empirical parameters to the inelastic strain rate, expressed as follows:

$$\dot{\varepsilon}_{\mathrm{inelastic}}\ \mathrm{s}^{-1} = 0.1\left|\frac{\sigma(\mathrm{MPa})(1 + 1000 \times \varepsilon_{\mathrm{inelastic}})^{\mathrm{m}}}{f(\mathrm{pct\ C})\left(\frac{T(\mathrm{K})}{300}\right)^{-5.52}}\right|^{\mathrm{n}} \qquad [11]$$

$$f(\mathrm{pct\ C}) = 1.3678 \times 10^{4}(\mathrm{pct\ C})^{-5.56\times10^{-2}}$$

$$m = -9.4156 \times 10^{-5}T(\mathrm{K}) + 0.3495$$

$$n = \left(1.617 \times 10^{-4}T(\mathrm{K}) - 0.06166\right)^{-1}$$

The austenite model,[13] given in the following equation, was developed as a curve fit to measurements made by Wray[14,15] and creep tests by Suzuki *et al.*[20]:

$$\dot{\varepsilon}_{\mathrm{inelastic}}\left(\mathrm{s}^{-1}\right) = f(\mathrm{pct\ C})\left[\sigma(\mathrm{MPa}) - f_1(T(\mathrm{K}))\varepsilon_{\mathrm{inelastic}}\left|\varepsilon_{\mathrm{inelastic}}\right|^{f_2-1}\right] \times \exp\left(\frac{-4.465 \times 10^{4}(\mathrm{K})}{T(\mathrm{K})}\right) \qquad [12]$$

$$f_1(\mathrm{T}(K)) = 130.5 - 5.128 \times 10^{-3}T(\mathrm{K})$$

$$f_2(\mathrm{T}(K)) = -0.6289 + 1.114 \times 10^{-3}T(\mathrm{K})$$

$$f_3(\mathrm{T}(K)) = 8.132 - 1.54 \times 10^{-3}T(\mathrm{K})$$

$$f(\mathrm{pct\ C}) = 4.655 \times 10^{4} + 7.14 \times 10^{4}(\mathrm{pct\ C}) + 1.2 \times 10^{5}(\mathrm{pct\ C})^{2}$$

where temperature is above the solidus, and the liquid model is used. The liquid is modeled as an elastic, perfectly plastic material with an elastic modulus of 10 GPa, a low yield stress of 0.01 MPa, and Poisson ratio of 0.3. The validity of using this method is found elsewhere.[73]

The effectiveness of using separate constitutive model for austenite and delta-ferrite to predict the tensile behavior of the Wray[14,15] and Suzuki *et al.*[20] experiments has been shown elsewhere as well.[77] Figure 4[77] shows that the constitutive models for delta-ferrite and austenite match well with tensile data from Wray for samples strained to 5 pct.

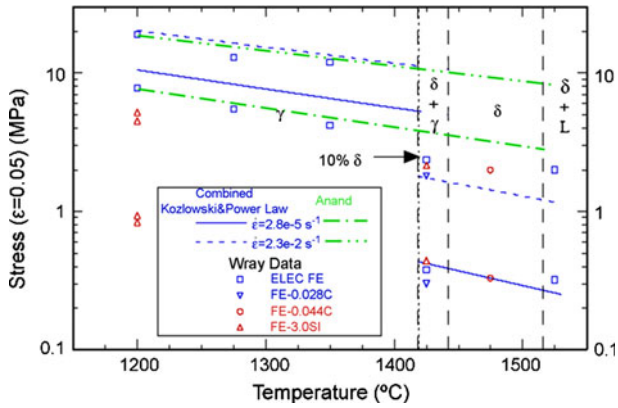

Fig. 4—Constitutive model performance compared to measured data.[77]

This figure also shows that delta-ferrite and mixtures of delta-ferrite and austenite are both considerably weaker than austenite alone. No clear transition was found for the stress magnitude during the phase transformation other than a steep increase in the stress at low delta-ferrite phase fractions. This is incorporated into the model by assuming that if the temperature is below the solidus and the delta-ferrite phase fraction exceeds 10 pct, then the delta-ferrite constitutive model is used (Eq. [11]). Otherwise, for temperatures below the solidus, the constitutive equation for austenite is used (Eq. [12]). If the temperature is greater than the solidus, then the elastic, perfectly plastic model of liquid is used.

E. *Other Thermal and Mechanical Properties*

The temperature-dependent thermal conductivity, specific heat, and TLE for the steel listed in Table I were obtained from the software package CON1D v.9.7.[78] The density was adopted from Harste and coworkers[79,80] as well as from Jimbo and Cramb[81] and depends on phase fractions. The thermal expansion coefficient was determined from the slope of the TLE curve. The elastic modulus was determined from data from Mizukami *et al.*[82]

The phase fractions were determined from CON1D using the segregation analysis procedure outlined by Won and Thomas.[83] The liquidus temperature was 1774.1 K (1500.95 °C), the solidus temperature was 1703.25 K (1430.1 °C), and the peritectic reaction occurs at 1759.55 K (1486.4 °C). The phase fraction history, thermal conductivity, specific heat, density, thermal expansion coefficient, and elastic modulus for the steel in Table I along with the determining equations for determining each property are given in the appendix.

F. *Finite Element Implementation*

The governing differential equations defined at the integration points in each element by the results of the constitutive (Eqs. [11] and [12]) are transformed into two integrated equations by invoking the backward Euler method and are solved by using a specialized Newton-Raphson method[10,13,84] The updated global equilibrium equations then are solved using the nonlinear procedures in the commercial software ABAQUS v. 6.9-1.[17] This approach has been implemented successfully[16,57] and has been validated by matching temperature and stress in the semianalytical solidification problem posed by Weiner and Boley.[63] The modeled domain, shown in Figure 5, uses 35,100 4-node linear axisymmetric finite elements for the upper part, lower part, ZrO_2 layer, and steel melt.

The mesh resolution was variable with those regions of the melt that solidify with 0.25 × 0.25 mm elements that transition gradually in regions that remain all liquid to 5.2 × 5.2 mm elements at the container wall. These variable element sizes were chosen to determine the stress and temperature gradients reasonably in the shell during solidification without incurring a large computation cost. Each simulation required ~11 hours central processing unit time on a 3.1-GHz, 64-bit personal computer.

G. *Boundary Conditions*

The radial displacement of the upper and lower parts is restricted at the centerline because of symmetry. Restriction of the vertical direction displacement is enforced at the top edge of the lower and upper parts to impose the physical restraints of the hydraulic cylinder and welded steel plate. Zero traction boundary conditions were applied to the steel melt at the top, right, and bottom edges. Zero heat flux boundary conditions are applied at the line of symmetry as well as at the bottom and right edge of the melt.

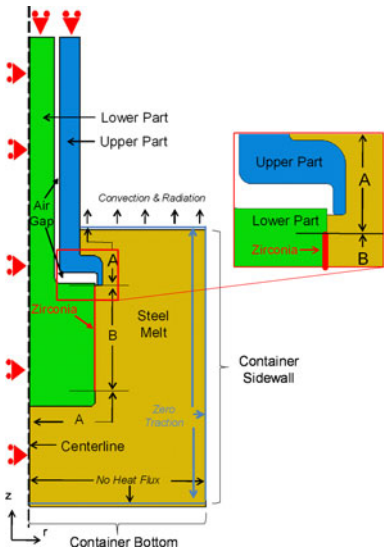

Fig. 5—Domain and boundary conditions of computational model of SSCC test.

Immersion of the test body is modeled by varying the heat-transfer coefficient (HTC) between the steel melt and the SSCC body with time and position. The origin of the model is located in the lower left corner. The interface of the test body and steel melt is treated with a Langrangian reference frame fixed on the test body in which the melt moves in the positive z-direction upward along the test body. At time $t = 0$ seconds, the bottom edge of the test body is 0.04 m from the origin. The three distinct regions in Figure 5 of the two test body–melt interfaces indicate the use of different coefficients of friction and HTC values. Assuming that the immersion velocity V_z is 0.1 m/s, the interfacial boundary conditions are expressed as follows:

$$\text{HTC}\left(\frac{\text{W}}{\text{m}^2\text{K}}\right) = \begin{cases} 0, & 0.040\ \text{m} > V_z \times t > 0 \\ 1850, & 0.047\ \text{m} \geq V_z \times t \geq 0.040\ \text{m} \\ 2500, & 0.088\ \text{m} > V_z \times t > 0.047\ \text{m} \\ 1850, & 0.110\ \text{m} \geq V_z \times t \geq 0.088\ \text{m} \\ 0, & V_z \times t > 0.110 \end{cases} \quad [13]$$

These boundary conditions indicate that the bottom surface of the lower part touches the melt at 0.4 seconds into the simulation and was chosen to verify the immersion effect on the melt and cylinder thermocouple measurements. The melt thermocouple touches the top surface of the melt at 0.7 seconds, and complete immersion occurs at 1.1 seconds. The HTC values were selected to match thermocouple measurements and solidified shell thickness contours best and are implemented into ABAQUS using a GapCon (Dusseldorf, Germany) subroutine. Convection and radiation from the top surface of the steel melt is simulated by assuming a HTC of 10 $\text{W/m}^2\text{/K}$ and an emissivity of 0.28 to ambient air at 303 K (30 °C).

The frictional interaction between the SSCC body and melt is separated into two distinct regions. The coefficient of friction between the steel melt and ZrO_2 was assumed to be 0.4 (labeled "B" in Figure 5). The coefficient of friction between the steel melt and all other interfacial regions was assumed to be 0.3 (labeled "A" in Figure 5).

VI. RESULTS

Because of the hostile, high-temperature environment of the solidifying steel experiment, only a few measurements are possible. Without an accurate model, this data is difficult to interpret. The first step in a complete interpretation of the data is to ensure that the model simultaneously matches all experimental measurements, including thermocouple temperature histories, final solidified shell thickness profile, reaction force history, and the location of cracks.

A. *Temperature*

Temperature has a great influence on stress during solidification, so it is not possible to predict stresses

without first achieving accurate temperature histories. Matching the measured cylinder temperatures is important to verify that reasonable thermal properties and boundary conditions are being used. A comparison of the thermocouple measurements and the corresponding simulated nodal temperature histories in the SSCC cylinder body is given in Figure 6(a). The difference between the simulation and the cylinder thermocouple TC-2 is less than the difference between the two measurements. Differences between the measurements may be caused by asymmetry in the placement of the thermocouples.

Note that a short delay occurs in the onset of increasing temperature in the cylinder. This delay is a result of immersion of the SSCC body. The initial temperature of the measurements is near 313 K (40 °C) even though room temperature was closer to 303 K (30 °C). This can be attributed to the SSCC body being suspended over the melt for a time period before the experiment began and being heated slightly from convection and radiation from the steel melt. The simulation of the melt temperature (Figure 6(b)) closely matches both measurements at early times. The sudden increase in the melt thermocouple, TM-1, around 10 seconds and the decrease of TM-2 around 16 seconds is because of thermocouple failure.

Figure 7 labels different regions of the interface between the melt and the test cylinder around the interior perimeter of the shell. Starting at the melt surface, the interface includes the melt contacting the upper part, air gap, lower part, ZrO_2 layer, and the bottom of the lower part. Figure 8 plots temperature along this interface at different times.

Figure 8 reveals that the shell temperature at 7 seconds is still slightly above the solidus temperature at region "6." At 7.1 seconds, the entire interface has cooled below the solidus temperature. For later times of 15 and 25 seconds significant additional cooling of the shell is only found in regions 1, near the top surface of the melt, and at regions 8 and 9, where the ZrO_2 layer exists.

Figure 9 shows relevant temperature contours, which includes a mirrored image to give a two-dimensional, cross-sectional representation, along with a close-up of the melt at the interface with the upper part at the end of the simulation and a scale representation of the shell. The contours represent the liquidus, 10 pct solid

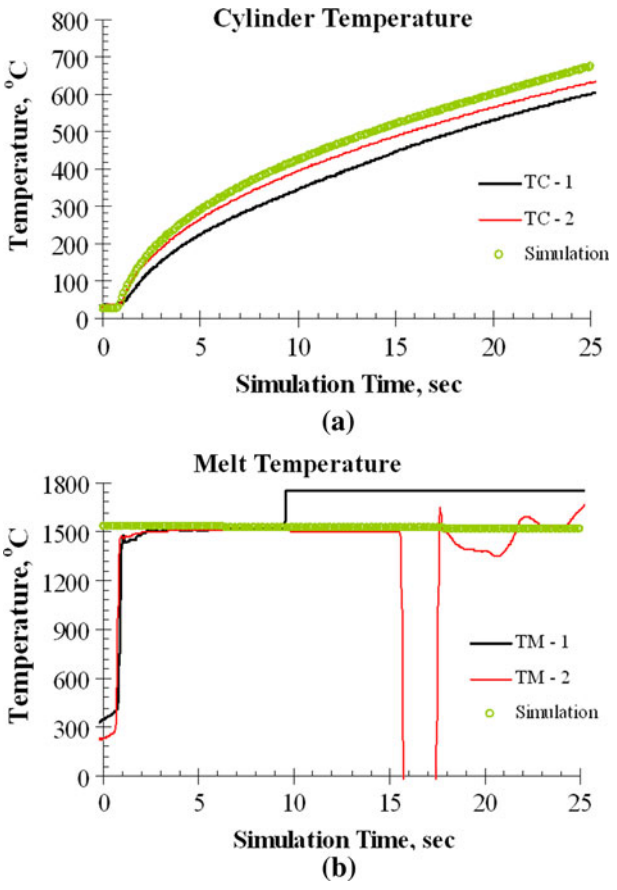

Fig. 6—Comparison of simulation and experimental measurements: (*a*) melt and (*b*) cylinder thermocouples.

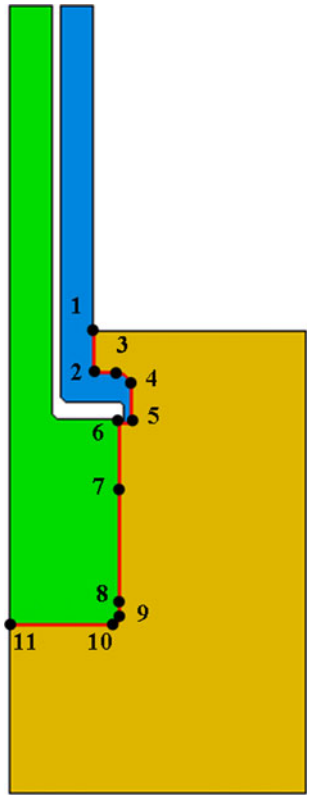

Fig. 7—Interfacial demarcation.

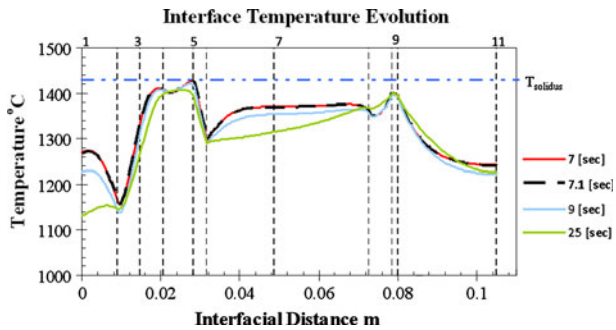

Fig. 8—Interface temperature for different simulation times.

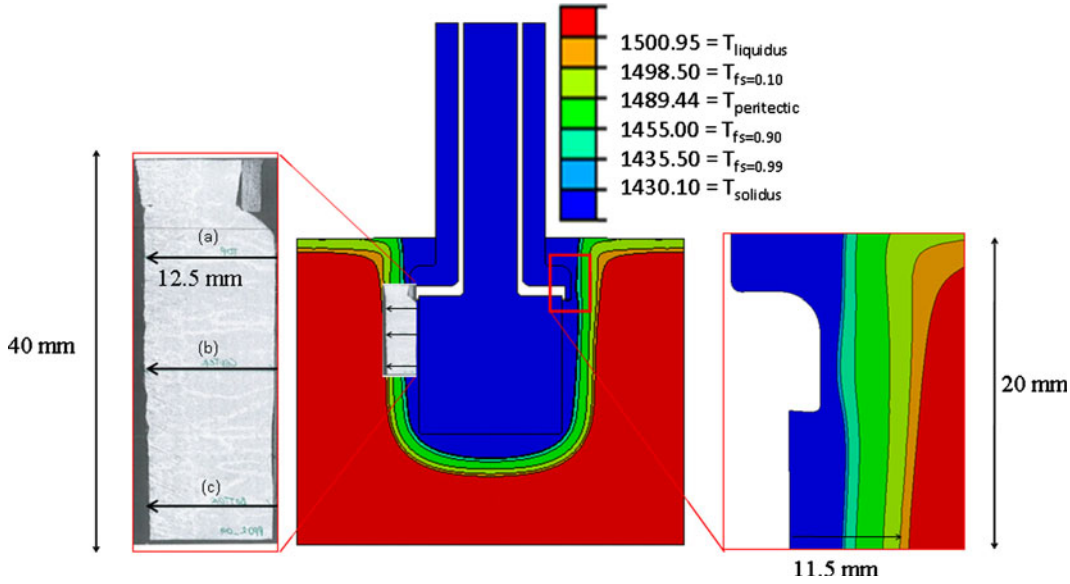

Fig. 9—Temperature contour at 25 s including shell and thickness measurement locations.

fraction, peritectic, 90 pct solid fraction, 99 pct solid fraction, and solidus temperatures.

Following the shape of the 10 pct solid fraction contour, it is apparent that the shape is similar to the photo of the test after it has been removed from the melt, including the formation of solid shell at the melt–air interface. Also, note that the distance from the thin vertical section of the upper part to the solidus contour is relatively thin.

B. *Shell Thickness*

The thickness of the shell was measured at three locations on eight equally spaced cut sections of the odd-numbered specimens pictured in Figure 3. Figure 9 also shows the specimen orientation and the three shell thickness measurement locations, denoted (a), (b), and (c). The shell thickness measurements in Table II average 12.5 ± 0.9 mm. The standard deviation is nearly 10 pct at location (a), which is nearest to the thin section of the upper part. The other regions show more uniformity.

The simulated shell thickness from the axisymmetric analysis was based on the temperature for 10 pct solid fraction. At the measured locations (a), (b), and (c), the predicted shell thickness is 11.5, 11.0, and 10.8 mm, respectively. It is unlikely that the HTCs were inappropriate because the model overpredicted the cylinder temperature thermocouple measurement. The most likely explanation is the neglect of liquid convection and heat extraction in the steel melt pool and subsequent cooling of the shell to room temperature. Including these effects might make the good match of the shell thickness distribution even better.

C. *Temperature and Stress Profiles in the Shell*

The highly nonlinear constitutive behavior of the steel and different interfacial heat-transfer conditions result in drastically different temperature and stress profiles at different times and sections through the solidified shell, such as those given in Figure 10.

Table II. Shell Thickness Measurements

	Measured Shell Thickness (mm)			
0.315 pct C	(a)	(b)	(c)	Mean
Cut section	—	—	—	—
S01	11.6	12.9	12.1	12.2
S03	11.3	11.6	12.2	11.7
S05	11.3	11.7	11.9	11.6
S07	13.0	12.7	12.7	12.8
S09	14.2	13.5	13.1	13.6
S11	14.3	13.8	13.6	13.9
S13	12.7	12.6	12.6	12.6
S15	11.8	11.6	12.0	11.8
Mean value	12.5	12.5	12.5	12.5
Standard deviation	1.2	0.9	0.6	0.9

The surface temperature at the interface with the upper part, cuts UP1 and UP2, cools rapidly to ~1673 K (1400 °C) but does not decrease much more during the test as the shell grows and lowers the temperature gradient. Stress is high in the solid austenite layer near the surface and drops sharply to nearly zero in the liquid. The different z-stress profiles taken at different horizontal cuts, shown in Figure 10, all drop to near zero in the two-phase liquid–solid region and liquid. The stress in the fully solidified region is much greater than zero and is a reflection of variation in the solid shell thickness as shown in Figure 9.

The surface temperature at the interface with the lower part, cuts LP1 and LP2, continues to drop for the duration of the test. The temperature gradients remain more uniform and the shell grows much thicker. This results in lower magnitude stress levels as the stress is distributed across a relatively thicker shell.

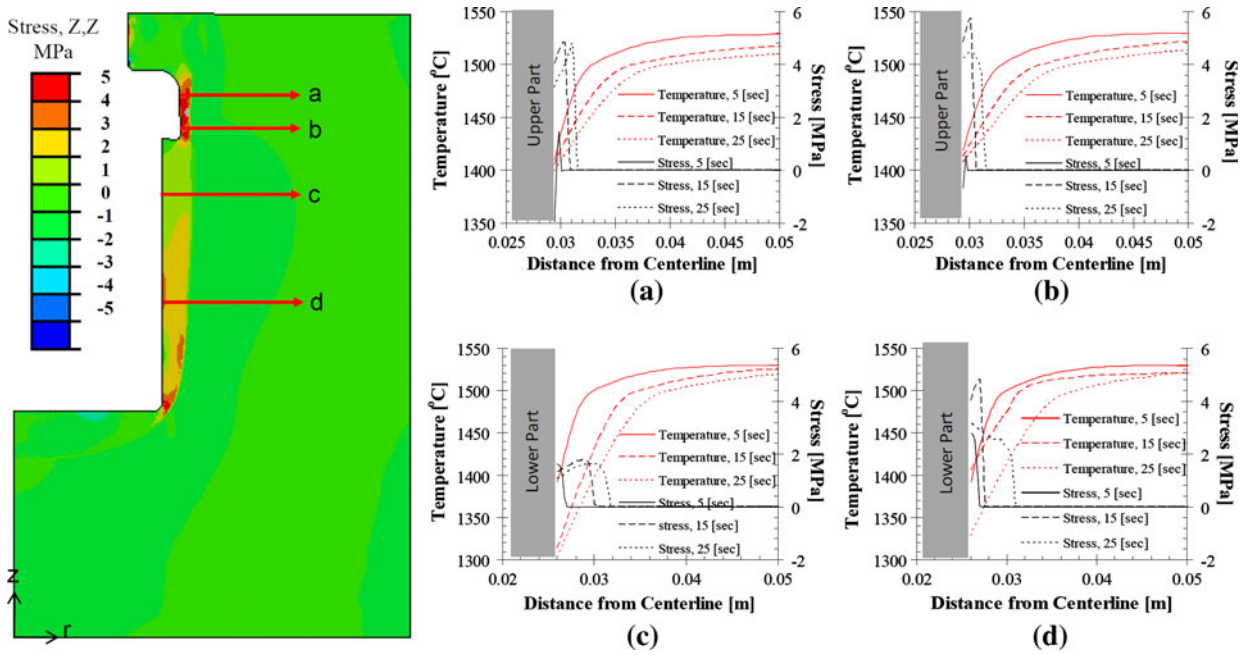

Fig. 10—Temperature and *z*-direction stress profiles for different locations and times within the shell.

D. *Force*

During the simulation, the force that the shell exerts on the SSCC body is counteracted by an imposed reaction to maintain the upper and lower parts at their original positions. This force is determined by summing the individual nodal reaction forces in the z-direction at nodes at the top edge of the lower part. The corresponding sum across the upper part matched within the ~0.1 pct numerical error to maintain equilibrium.

The simulated reaction force and the measured force are compared in Figure 11.

The measured force increases slowly from 0 to 4 seconds, then decreases linearly to a low of –806 N at 16 seconds, before linearly increasing and leveling off at ~−500 N until the end of the experiment. The simulated force remains at nearly 0 until 7 seconds and then abruptly decreases to the force level of the experiment and continually increases. The simulation does not see the gradual increase and leveling off of force levels as in the experiment.

The sudden decrease of the simulation force at 7.1 seconds is a reflection of the modeling approach. Recall, the interfacial temperature of the shell does not cool below the solidus temperature until 7.1 seconds, as shown in Figure 8. The model assumes a low yield stress when the temperature is above the solidus. The nonzero measured stress during this initial time indicates that interlocking dendrites within the two-phase liquid–solid region must give it some strength, which is not part of the current model.

This finding is important because the temperature and strength of a small region of the interface seems to determine the measured force output, even when other regions of the shell at the interface are more than 100 K below the solidus temperature, have high complex stress profiles, and are capable of carrying much higher loads levels.

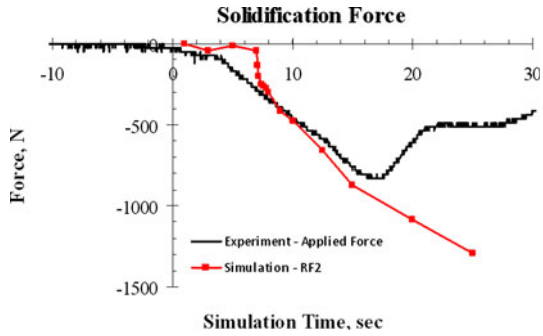

Fig. 11—Comparison of experimental and simulated force curves.

E. *What is the SSCC Measuring?*

The same four cuts of the shell, indicated in Figure 10, at 10 seconds solidification were analyzed to determine how the reaction force at the boundary condition displacement relates to the local force in a solidifying shell.

Each horizontal cut, beginning at the interface with the SSCC test body consists of a solid shell, a two-phase liquid–solid region, and then liquid. Table III summarizes the individual contributions to the total force in the solidifying shell using the methodology of extracting forces from the NFORC2 variable. Recall that, at 10 seconds, the simulated reaction force at the displacement boundary condition was –476 (N). As indicated by Table III, a clear disagreement was noted in what the force is in the fully solidified region and in the total force.

F. *What Does the Reaction Force at the Displacement Boundary Condition Indicate?*

At contacting surfaces, the shear and normal components of force balance the nodal force to satisfy equilibrium as follows[17]:

$$\text{CSHEARF}_i + \text{CNORMF}_i = \text{NFORC}_i \qquad [14]$$

where CSHEARF and CNORMF are the nodal shear and normal contact forces in the i direction and are ABAQUS field variables at contact surfaces.

The interfacial forces are determined from the shear stress generation caused by contact pressure and friction at the interface according to the following equation:

$$\tau_i = \tau_{\text{eq}} \frac{\dot{\gamma}_i}{\dot{\gamma}_{\text{eq}}} \qquad [15]$$

Table III. Summary of Forces in Cuts Indicated in Figure 12 at 10 Seconds

Cut	Fully Solid (N)	Mushy Zone (N)	Fully Liquid (N)	Total (N)
UP1	–498.16	–85.79	–15.04	–589.99
UP2	–442.35	1.35	–15.48	–456.48
LP1	–588.1	7.26	–10.28	–591.12
LP2	–1017.47	3.11	–12.68	–1027.04

where τ_i is the interface shear stress in the slip direction i, τ_{eq} is the equivalent interface shear stress, $\tau_{\text{eq}} = \mu p$, where μ is the coefficient of friction, p is the contact pressure, $\dot{\gamma}_i$ is the slip rate, and $\dot{\gamma}_{\text{eq}}$ is the magnitude of the slip velocity, which is expressed as follows:

$$\dot{\gamma}_{\text{eq}} = \sqrt{(\dot{\gamma}_1)^2 + (\dot{\gamma}_2)^2}$$

For this two-dimensional, axisymmetric problem, tangential motion of the surfaces during contact are only relative between two surfaces. Therefore, i is renamed "slip."

Figures 10 and 12 and the data in Table III show nonuniformity in the shell stress and subsequently the strength when strictly analyzing horizontal cuts through arbitrary locations in the shell. Using the interface demarcation as shown in Figure 7, the total accumulated interfacial force beginning at the melt surface and proceeding in the negative z direction is plotted.

At contacting surfaces, the NFORC resulting from elemental stresses is balanced by CNORMF and CSHEARF according to Eq. [14].

Recall that at fixed-displacement boundaries, NFORC balance RFs as follows:

$$\text{NFORC}_i + \text{RF}_i = 0 \qquad [16]$$

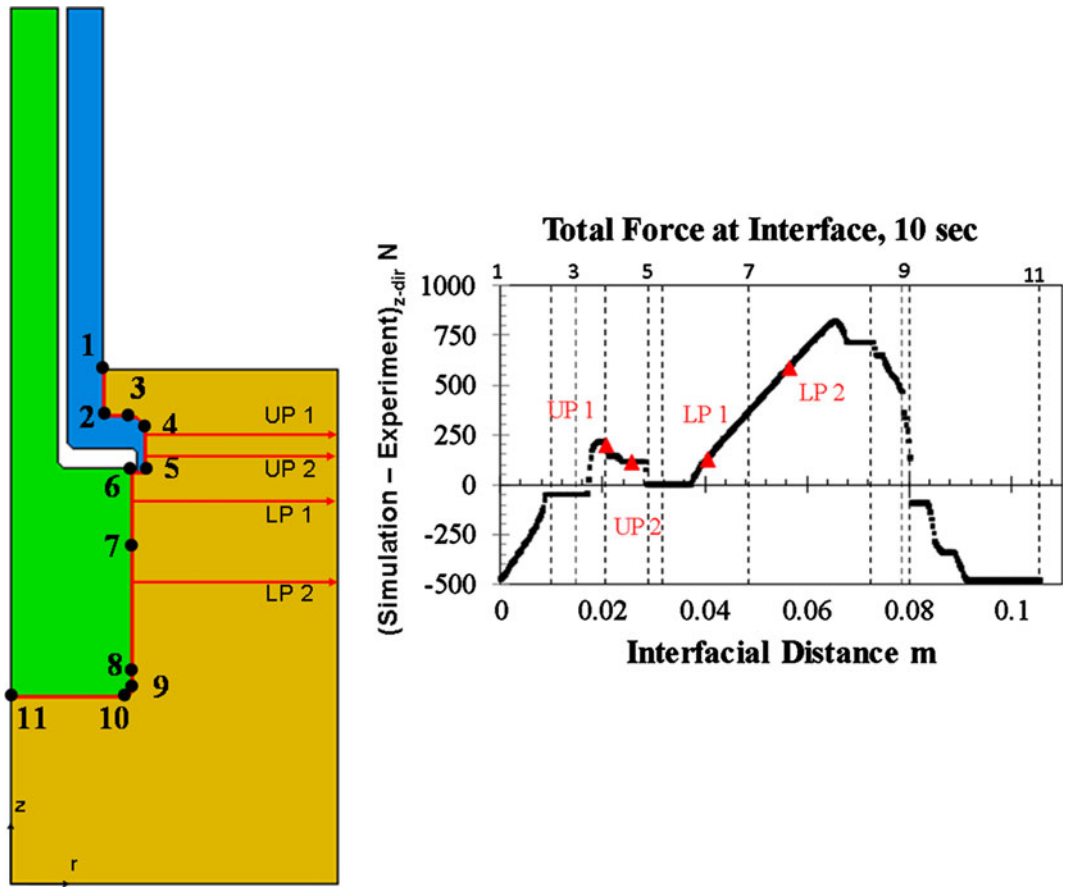

Fig. 12—Balance of contact and reaction force along the interface compared with horizontal cut force values from Fig. 12.

The location where the interfacial forces balance the reaction force, far from the interface, in the z-direction at any node along the interface then can be calculated as follows:

$$F_{\text{balance}} = \sum_{i=1}^{k} \left(\text{CNORMF}_{2,i} + \text{CSHEARF}_{2,i}\right) + \text{RF}_2 \quad [17]$$

where $i = 1$ is the first node along the interface and the force at any node k can be computed. By using this method, analyzing where Eq. [17] is zero, indicates the node(s) that are driving the determination of the reaction force at the top surface with the displacement boundary condition.

As indicated by Figure 12, offset by the reaction force at 10 seconds, –476 (N) lie along the same curve. Most important, however, is that only one part of Figure 12 exists where the contact forces and reaction force balance.

This traverses regions 6, 7, and part of 8 of Figure 7 and corresponds to the section of the shell that connects the upper and lower parts. At 10-seconds solidification time, the shell has formed a gap with the SSCC body in these regions. Recall that region 6 also corresponded to where the temperature of the shell at the interface was highest. The portion of the shell that connects the upper and lower parts is determining the reaction force being measured by the experiment.

Figure 12 also shows that the cuts of the shell have a solidification force equal to the net interfacial force. This finding indicates that the shell strength at locations other than the connection between the upper and lower parts include the effects of contact pressure and shear stresses that develop during the cooling/shrinking of the shell and the heating/expanding of the test cylinder.

The shell that connects the upper and lower parts is the shell strength being measured by the SSCC experiment. This region also corresponds to where the shell is hottest and therefore weakest. So, for this particular case, the measured force is a reflection of the shell at its weakest point and does not reflect the strength of the shell at a cut at the interface with the lower part as indicated by previous investigations.[12]

VII. HOT TEARING

As a first step in determining whether the simulation can match micrographs that show failures, the contour of the inelastic strain perpendicular to the dendrite growth direction is plotted and compared with micrographs of the same alloy that developed defects. Figure 13 superimposes the 90 pct and 99 pct solid fraction temperature, which is the range within the

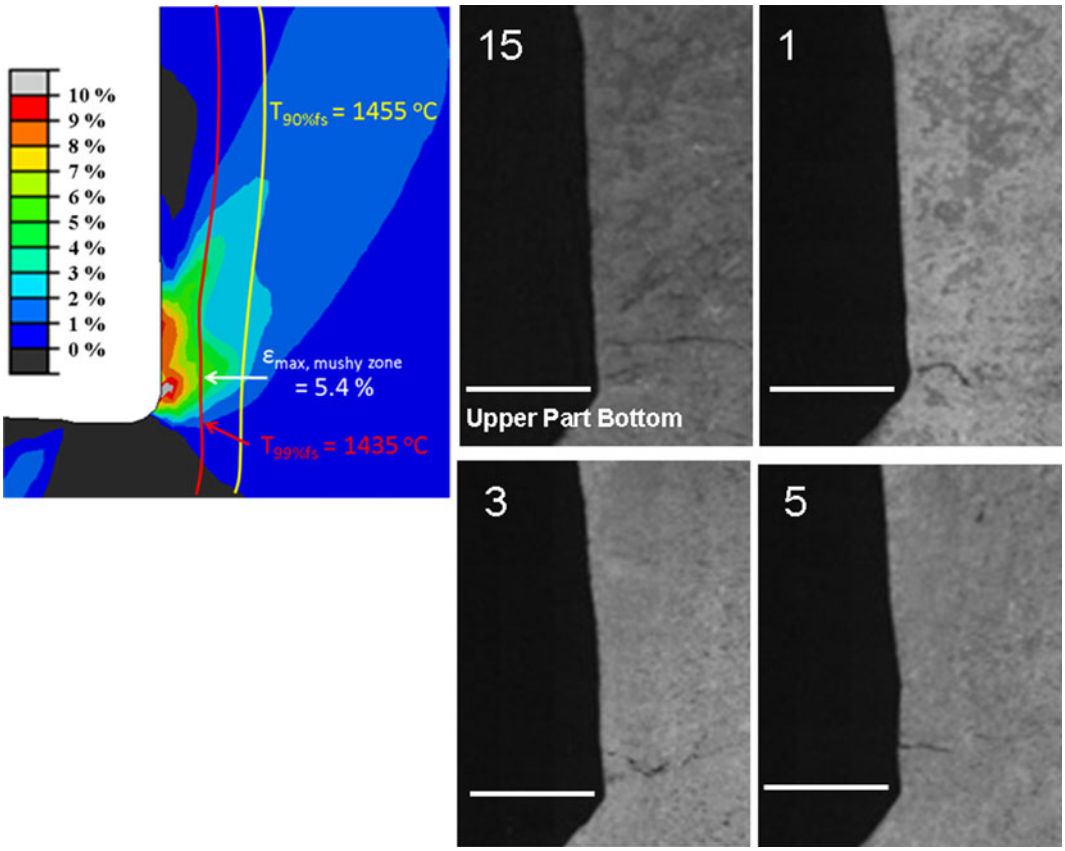

Fig. 13—Simulation determination of likely hot tear formation and comparison with experimental samples.

dendritic solid–liquid two-phase region that is often associated with that area where hot tears tend to occur. It is shown that the inelastic strain in the two-phase liquid–solid region is a maximum of 5.4 pct, which is a high value in comparison with critical strain values of hot tearing published in the relevant literature. Comparing this high inelastic strain with micrographs of the SSCC test, it is easily shown that hot tears tend to form in this area. Good agreement is found between the simulation and the experiment.

VIII. CONCLUSIONS

A transient two-dimensional, axisymmetric finite-element model of the SSCC test has been developed. This model can successfully simulate thermal-mechanical behavior during steel solidification, owing to its agreement with measurements of temperature, shell thickness, axial force, and the location of hot-tear cracks. This finding demonstrates that the constitutive equations assumed in the model are reasonable. By simulating shell growth for a given steel in a SSCC test, the model showed that the previous understanding of the test operation was incorrect. Instead of measuring the solidification force at any arbitrary cut of the shell, the experiment measures the strength of the shell that forms a connection between the upper and lower parts, which also tends to be the location where the shell is hottest. The model could indicate the development of nonuniform stress profiles at different locations of a solidifying shell in addition to predicting locations accurately where hot-tear cracks are likely to form. This modeling tool can be applied to predict temperature, stress, location, and time of hot-tear crack formation in steel cast at the commercial scale.

APPENDIX A–MATERIAL PROPERTIES OF STEEL MELT AND SSCC TEST BODY

The temperature dependent thermal conductivity (below) was taken from Harste *et al.*[80] and Jimbo and Cramb[81]

$$
\begin{aligned}
k[\mathrm{W/m/K}] &= k_\alpha f_\alpha + k_\gamma f_\gamma + k_\delta f_\delta + k_l f_l \\
k_\alpha &= \left[80.91 - 9.9269 \times 10^{-2} T[^\circ\mathrm{C}] \right. \\
&\quad \left. + 4.613 \times 10^{-5} T[^\circ\mathrm{C}]^2 \right] \left[1 - a_1[\text{pct C}]^{a_2}\right] \\
k_\gamma &= 21.6 - 8.35 \times 10^{-3} T[^\circ\mathrm{C}] \\
k_\delta &= \left[20.14 - 9.313 \times 10^{-3} T[^\circ\mathrm{C}]\right] \left[1 - a_1[\text{pct C}]^{a_2}\right] \\
k_l &= 39.0 \\
a_1 &= 0.7425 - 4.385 \times 10^{-4} T[^\circ\mathrm{C}] \\
a_2 &= 0.209 + 1.09 \times 10^{-3} T[^\circ\mathrm{C}]
\end{aligned}
\qquad [A1]
$$

where k_α, k_γ, k_δ, and k_l are the conductivities of the α-ferrite, austenite, δ-ferrite and liquid phases, f_α, f_γ, f_δ, and f_l are phase fractions for α-ferrite, austenite, δ-ferrite and liquid, a_1 and a_2 are empirical parameters, T is temperature °C and pct C is weight percent carbon.

Likewise, the specific heat curve is also fitted from data conglomerated by Harste.[80]

$$
\begin{aligned}
c_p[\mathrm{J/kg}] &= c_{p,\alpha} f_\alpha + c_{p,\gamma} f_\gamma + c_{p,\delta} f_\delta + c_{p,l} f_l \\
c_{\mathrm{p},\alpha} &= \begin{cases}
-10068.18 + (5.98686 \times T[\mathrm{K}]) + \left(\frac{5217657 \times 10^3}{(T[\mathrm{K}])^2}\right), \\
\qquad T[\mathrm{K}] > 1060 \\
34871.21 - (32.02658 \times T[\mathrm{K}]), \\
\qquad 1042 < T[\mathrm{K}], 1060 \\
-11501.07 + (12.476362 \times T[\mathrm{K}]), \\
\qquad 1000 < T[\mathrm{K}] < 1042 \\
-4720.324 + (4.583364 \times T[\mathrm{K}]) + \left(\frac{1109483}{(T[\mathrm{K}])^2}\right), \\
\qquad 800 < T[\mathrm{K}] < 1000 \\
504.8146 - (0.1311139 \times T[\mathrm{K}]) + \left(\frac{5187583.4}{(T[\mathrm{K}])^2}\right) \\
\qquad + \left(0.000448666 + (T[\mathrm{K}])^2\right), T[\mathrm{K}] < 800
\end{cases} \\
c_{p,\delta} &= 441.3942 + (0.17744236 \times T[\mathrm{K}]) \\
c_{p,l} &= 429.8495 + (0.1497802 \times T[\mathrm{K}]) \\
c_{\mathrm{p},l} &= 824.6157
\end{aligned}
\qquad [A2]
$$

where $c_{p,\alpha}$, $c_{p,\gamma}$, $c_{p,\delta}$, and $c_{p,l}$ is the specific heat of the α-ferrite, austenite, δ-ferrite and liquid phases respectively and T is temperature in K.

The latent heat, L_f, was assumed to be 271,000 J/kg. The effective specific heat, c_p^*, is used to distribute the latent heat in the mushy zone according to the increase in the solid fraction, f_s as the shell cools from the liquidus to the solidus temperature according to Eq. [A3]

$$
c_p^* = c_p - L_f \frac{df_\mathrm{s}}{dT} \qquad [A3]
$$

The thermal linear expansion (TLE) is determined from solid phase density measurements of Harste[80] and Jablonka[81] and by Jimbo and Cramb[82] for liquid steels. Equations for both TLE and density are given in Eq. [4].

$$
\mathrm{TLE}[-] = \sqrt[(3)]{\frac{\rho(T_\mathrm{ref})}{\rho(T)}} - 1
$$

where

$$
\begin{aligned}
\rho\left[\mathrm{kg/m^3}\right] &= \rho_\alpha f_\alpha + \rho_\gamma f_\gamma + \rho_\delta f_\delta + \rho_l f_l \\
\rho_\alpha &= 7881 - 0.324 T[^\circ\mathrm{C}] - 3 \times 10^{-5} (T[^\circ\mathrm{C}])^2 \\
\rho_\gamma &= \frac{100(8106 - 0.51 T[^\circ\mathrm{C}])}{(100 - (\text{pct C}))(1 + 0.008(\text{pct C}))^3} \\
\rho_\delta &= \frac{100(8011 - 0.47 T[^\circ\mathrm{C}])}{(100 - (\text{pct C}))(1 + 0.013(\text{pct C}))^3} \\
\rho_l &= 7100 - 73(\text{pct C}) \\
&\quad - (0.8 - 0.09(\text{pct C}))(T(^\circ\mathrm{C}) - 1550)
\end{aligned}
\qquad [A4]
$$

where TLE is the thermal linear expansion, ρ_α, ρ_γ, ρ_δ, and ρ_l are the densities kg/m^3 of the α-ferrite, austenite, δ-ferrite and liquid phases and T is temperature °C. The TLE is converted to a thermal

expansion coefficient, α, by computing the slope of the TLE *vs* temperature curve. The reference temperature was chosen to be 300 °C with a reference TLE of -1.66×10^{-2}.

$$\alpha\left[\frac{1}{^{o}\mathrm{C}}\right] = \frac{\mathrm{TLE_{ref}} - \mathrm{TLE(T)}}{T_{\mathrm{ref}} - T} \qquad [A5]$$

NOMENCLATURE

B	volumetric force vector (N)
CNORMF	nodal normal contact force (N)
CSHEARF	nodal shear contact force (N)
c_p	specific heat (J/Kg/K)
c_p'	solid fraction-dependent specific heat (J/Kg/K)
$\underline{\underline{D}}$	fourth order isotropic tensor of elasticity (N/M^2)
E	elastic modulus (N/M^2)
F	force (N)
F_{balance}	deviation from force balance (N)
f(pct C)	empirical constant in Kozlowski III law ($MPa^{-f_3}\ s^{-1}$)
f_1	empirical constant in Kozlowski III law (MPa)
f_2	empirical constant in Kozlowski III law
f_3	empirical constant in Kozlowski III law
f_s	solid fraction
I	moment of inertia (Kg M^2)
I	second order identity tensor
$\underline{I}$	fourth order identity tensor
$\overline{\overline{K}}$	temperature-dependent thermal conductivity (W/M/K)
K_{B}	temperature-dependent bulk modulus (N/M^2)
L_{F}	latent heat (J/Kg/K)
L	restrained length (M)
M	empirical constant used in power Delta Law
N	empirical constant used in power Delta Law
NFORC	nodal force (N)
P	contact pressure (MPa)
RF	reaction force (N)
R	radial coordinate (M)
T	temperature (°C)
T_0	reference temperature (°C)
T_{ref}	reference temperature (°C)
T	time (s)
TLE	thermal linear expansion
$\mathrm{TLE_{ref}}$	reference thermal linear expansion
$\vec{u}$	displacement vector
V_Z	immersion velocity (m/s)
Z	vertical coordinate (m)
$\alpha(T)$	temperature-dependent coefficient of thermal expansion ($°C^{-1}$)
δ_{ij}	Kronecker's delta
δ_{max}	maximum displacement (m)
ε	total strain tensor
$\dot{\varepsilon}$	total strain rate tensor (s^{-1})
$\dot{\varepsilon}_{\mathrm{elastic}}$	elastic strain rate tensor (s^{-1})
$\dot{\varepsilon}_{\mathrm{inelatic}}$	inelastic strain rate tensor (s^{-1})
$\dot{\varepsilon}_{\mathrm{thermal}}$	thermal strain rate tensor (s^{-1})
$\dot{\gamma}$	slip rate tensor (s^{-1})
$\dot{\gamma}_{\mathrm{eq}}$	magnitude of the slip velocity (s^{-1})
μ	coefficient of friction; temperature-dependent shear modulus (MPa)
ρ	temperature-dependent density (Kg/m^3)
σ	stress tensor (MPa)
$\dot{\sigma}$	stress rate tensor (MPa)
τ	interface shear stress tensor (MPa)
τ_{eq}	equivalent interface shear stress (MPa)

REFERENCES

1. C. Bernhard and G. Xia: *Ironmaking Steelmaking*, 2006, vol. 33 (1), pp. 52–56.
2. C. Bernhard, H. Hiebler, and M. Wolf: *Ironmaking Steelmaking*, 2000, vol. 27, pp. 450–54.
3. C. Bernhard, W. Schutzenhofer, H. Hiebler, and M. Wolf: *Proc. 2nd Int. Conf. on Science and Technology of Steelmaking*, Swansea, U.K., 2001, p. 87.
4. C. Bernhard, H. Hiebler, and M. Wolf: *Rev. Metall., Cah. Inf. Tech.*, 2000, vol. 97, pp. 333–44.
5. C. Bernhard, H. Hiebler, and M. Wolf: *ISIJ Int.*, 1996, vol. 36, pp. S163–S166.
6. P. Ackermann, J.-D. Wagniere, and W. Kurz: *EPFL*, 1985, in press.
7. C. Bernhard, H. Hiebler, and M.M. Wolf: *ISIJ Int.*, 1996, vol. 36, pp. S163–S166.
8. R. Pierer, C. Bernhard, and C. Chimani: *La Revue de Métallurgie—CIT*, 2007, pp. 72–83.
9. J. Reiter, C. Bernhard, and H. Presslinger: *Met. Charact.*, 2008, vol. 59, pp. 737–46.
10. G. Gigacher, R. Pierer, J. Wiener, and C. Bernhard: *Adv. Eng. Mater.*, 2006, vol. 8 (11), pp. 1096–1100.
11. P. Ackermann, W. Kurz, and W. Heinemann: *Mat. Sci. Eng.*, 1985, vol. 75, pp. 79–86.
12. R. Pierer, C. Bernhard, and C. Chimani: *BHM*, 2005, vol. 150, pp. 163–69.
13. P. Kozlowski, B. Thomas, J. Azzi, and H. Wang: *Metall. Trans. A*, 1992, vol. 23A, pp. 903–18.
14. P.J. Wray: *Metall. Trans. A*, 1975, vol. 6A, pp. 1189–96.
15. P.J. Wray: *Metall. Trans. A*, 1976, vol. 7A, pp. 1621–27.
16. S. Koric and B. Thomas: *Int. J. Num. Met. Eng.*, 2006, vol. 66, pp. 1955–89.
17. ABAQUS User Manuals v6.9, Dassault Systèmes Simulia Corp., Providence, RI, 2009.
18. L. Hibbeler: Master's Thesis, The University of Illinois at Urbana, Champaign, IL, 2009.
19. K. Wiirmenberg: *Stahl Eisen*, 1978, vol. 98, pp. 254–59.
20. T. Suzuki, K.H. Tacke, and K. Schwerdtfeger: *Ironmaking Steelmaking*, 1988, vol. 15, pp. 90–100.
21. G. Shin, T. Kajitani, T. Suzuki, and T. Umeda: *Tetsu-to-Hagané*, 1992, vol. 78, pp. 587–93.
22. H. Mizukami, K. Nakajima, M. Kawamoto, T. Watanabe, and T. Umeda: *Tetsu-to-Hagané*, 1998, vol. 84, pp. 417–22.
23. H. Mizukami, S. Hiraki, M. Kawamoto, and T. Watanabe: *Tetsu-to-Hagané*, 1998, vol. 84, p. 763.
24. H. Mizukami, A. Yamanaka, and T. Watanabe: *Tetsu-to-Hagané*, 1999, vol. 85, pp. 592–98.
25. T. Umeda, J. Matsuyama, H. Murayama, and M. Sugiyama: *Tetsu-to-Hagané*, 1977, vol. 63, p. 441.
26. H. Suzuki, T. Nakamura, and T. Nishimura: *Final Report of Committee on Mechanics Related Behavior in Continuous Casting, ISIJ*, Tokyo, 1985, p. 87.
27. K. Miyazawa and K. Schwerdtfeger: *Ironmaking Steelmaking*, 1979, vol. 6, pp. 68–74.
28. T. Suzuki, K.H. Tacke, and K. Schwerdtfeger: *Metall. Trans. A.*, 1991, vol. 19A, pp. 2857–59.

29. Y. Sugitani, M. Nakamura, H. Kawashima, K. Kanazawa, H. Tomono, and M. Hashio: *Tetsu-to-Hagane*, 1982, vol. 68, pp. 149–52.
30. K. Wunnenberg and R. Flender: *Ironmaking Steelmaking*, 1985, vol. 12, pp. 22–29.
31. S. Nagata, T. Matsumiya, K. Ozawa, and T. Ohashi: *Tetsu-to-Hagane*, 1990, vol. 76, pp. 214–21.
32. H. Mizukami, A. Yamanaka, and T. Watanabe: *ISIJ Int*., 2002, vol. 42 (9), pp. 964–73.
33. G. Xia, J. Zirngast, H. Hiebler, and M.M. Wolf: *Proc. Conf. on Continuous Casting of Steels in Developing Countries*, The Chinese Society for Metallurgy, Beijing, China, 1993, p. 200.
34. H. Hiebler and M.M. Wolf: *ISIJ Int*., 1993, vol. 6, p. 1132.
35. H. Hiebler, J. Zirngast, C. Bernhard, and M. Wolf: *Steelmaking Conf. Proc*., 1994, vol. 77, p. 405.
36. H. Hiebler and C. Bernhard: *Steel Res*., vol. 69 (8–9), pp. 349–55.
37. C. Bernhard, H. Hiebler, and M. Wolf: *Revue Métallurgi CIT*, 2000, pp. 333–44.
38. B.G. Thomas: *ASM Handbook - Defects*, vol. 22, ASM, Materials Park, OH, 2008, pp. 449–61.
39. A. Palmaers: *Met. Rep. CRM*, 1978, vol. 53, p. 23.
40. J. Hertel, H. Litterscheidt, U. Lotter, and H. Pircher: *Rev. Met.-CIT*, 1992, vol. 89, p. 73.
41. M. Rappaz, I. Farup, and J.M. Drezet: *Proc. Merton C. Flemmings Symp. on Solidifcation and Materials Processing*, 2001, pp. 213–22.
42. M. Rappaz, J.M. Drezet, and M. Gremaud: *Metall. Mater. Trans. A*, 1999, vol. 30A, pp. 449–55.
43. T.W. Clyne and G.J. Davies: *Solid Cast of Metals*, TMS, London, U.K., 1979, pp. 275–78.
44. U. Feurer: *Quality Control of Engineering Alloys and the Role of Metals Science*, Delft University of Technology, Delft, The Netherlands, 1977, pp. 131–45.
45. L. Katgerman: *J. Met*., 1982, vol. 34 (2), pp. 46–49.
46. D.G. Eskin and L. Katgerman: *Metall. Mater. Trans. A*, 2007, vol. 38A, pp. 1511–19.
47. B. Magnin, L. Maenner, L. Katgerman, and S. Engler: *Mater. Sci. Forum*, 1996, vols. 217–222, pp. 1209–14.
48. L. Zhao, Baoyin, N. Wang, V. Sahajwalla, and R.D. Pehlke: *Int. J. Cast Met. Res*., 2000, vol. 13 (3), pp. 167–74.
49. Y.M. Won, T.J. Yeo, D.J. Seol, and K.H. Oh: *Metall. Mater. Trans. B*, 2000, vol. 31B, pp. 779–94.
50. M. Braccini, C.L. Martin, M. Suery, and Y. Brechet: *Modelling of Casting*, Welding and Advanced Solidification Processes IX, Shaker Verlag, Aachen, Germany, 2000, pp. 18–24.
51. N.N. Prokhorov: *Russ. Castings Prod*., 1962, vol. 2, pp. 172–75.
52. E. Niyama: *Japan–US Joint Seminar on Solidification of Metals and Alloys*, Japan Society for Promotion of Science, Tokyo, Japan, 1977, pp. 271–82.
53. J.F. Grandfield, D.J. Cameron, and J.A. Taylor: *Light Metals 2001*, TMS, Warrendale, PA, 2001, pp. 895–901.
54. J.-M. Drezet and M. Rappaz: *Light Metals 2001*, TMS, Warrendale, PA, 2001, pp. 887–93.
55. C.H. Dickhaus, L. Ohm, and S. Engler: *Trans. Am. Foundry Soc*., 1994, vol. 101, pp. 677–84.
56. J. Langlais and J.E. Gruzleski: *Mater. Sci. Forum*, 2000, vols. 331–337, pp. 167–72.
57. D.J. Lahaie and M. Bouchard: *Metall. Mater. Trans. B*, 2001, vol. 32B, pp. 697–705.
58. J.A. Williams and A.R.E. Singer: *J. Inst. Met*., 1968, vol. 96, pp. 5–12.
59. B. Rogberg: *Scand. J. Metall*., 1983, vol. 12, pp. 51–66.
60. M. Suzuki, M. Suzuki, C. Yu, and T. Emi: *ISIJ Int*., 1997, vol. 37 (4), pp. 375–82.
61. P. Yavari, D.A. Miller, and T.G. Langdon: *Acta Metall*., 1982, vol. 30, pp. 871–79.
62. T.W. Clyne and G.J. Davies: *Br. Foundryman*, 1981, vol. 74, pp. 65–73.
63. J.H. Weiner and B.A. Boley: *J. Mech. Phys. Solids*, 1963, vol. 11, pp. 145–54.
64. A. Grill, J.K. Brimacombe, and F. Weinberg: *Ironmaking Steelmaking*, 1976, vol. 3, pp. 38–47.
65. F. Wimmer, H. Thone, and B. Lindorfer: *ABAQUS Users Conf*., Urbana, IL, 1996.
66. F.G. Rammerstrofer, C. Jaquemar, D.F. Fischer, and H. Wiesinger: *Temperature Fields, Solidification Progress and Stress Development in the Strand During a Continuous Casting Process of Steel, Num. Meth. Therm. Probs*, Pineridge Press, Whiting, NJ, 1979, pp. 712–22.
67. J.O. Kristiansson: *J. Therm. Stresses*, 1984, vol. 7, pp. 209–26.
68. H. Zhu: Ph.D. Dissertation, The University of Illinois at Urbana, Champaign, IL, 1993.
69. J.R. Boehmer, G. Funk, M. Jordan, and F. Fett: *Adv. Soft. Eng*., 1998, vol. 29 (7–9), pp. 679–97.
70. I. Farup and A. Mo: *Metall. Mater. Trans. A*, 2000, vol. 31A, pp. 1461–72.
71. C. Li and B. Thomas: *Metall. Mater. Trans. B*, 2005, vol. 35B, pp. 1151–72.
72. J.M. Risso, A.E. Huespe, and A. Cardona: *Int. J. Num. Met. Eng*., 2006, vol. 65 (9), pp. 1355–77.
73. S. Koric, L. Hibbeler, and B. Thomas: *Int. J. Num. Met. Eng*., 2009, vol. 78, pp. 1–31.
74. C. Bernhard, R. Pierer, A. Tubikanec, and C. Chimani: *Continuous-Casting Innovation Session*, paper no. 06.03, CCR, 2004, pp. 1–9.
75. C. Bernhard and R. Pierer: *Mater. Sci. Technol*., 2006, vol. 1.
76. W. Kurz: *La Metallurgia Italiana, Lugio/Agosto*, 2008, vol. 7/8, pp. 56–64.
77. C. Li: Ph.D. Dissertation, The University of Illinois at Urbana, Champaign, IL, 2004.
78. Y. Meng and B. Thomas: *Metall. Mater. Trans. B*, 2003, vol. 34B, pp. 685–705.
79. K. Harste: Ph.D. Dissertation, Technical University of Clausthal, Zellerfeld Germany, 1989.
80. K. Harste, A. Jablonka, and K. Schwerdtfeger: *4th Int. Conf. Continuous Casting*, 1988, vol. 2, pp. 633–44.
81. I. Jimbo and W. Cramb: *Metall. Mater. Trans. B*, 1993, vol. 24B, pp. 5–10.
82. H. Mizukami, K. Murakami, and Y. Miyashita: *Tetsu-to-Hagane*, 1977, vol. 63 (146), p. S652.
83. Y. Won and B. Thomas: *Metall. Mater. Trans. A*, 2003, vol. 32A, pp. 1755–67.
84. A.M. Lush, G. Weber, and L. Anand: *Int. J. Plast*., 1989, vol. 5, pp. 521–49.